

# Topological junction states in graphene nanoribbons: A route to topological chemistry

Hazem Abdelsalam,<sup>\*,†,‡</sup> Domenico Corona,<sup>\*,¶</sup> Renebeth B. Payod,<sup>\*,§</sup> Mahmoud A. S. Sakr,<sup>\*,||</sup> Omar H. Abd-Elkader,<sup>\*,⊥</sup> Qinfang Zhang,<sup>\*,†</sup> and Vasil A. Saroka<sup>\*,¶,#,@</sup>

<sup>†</sup>*School of Materials Science and Engineering, Yancheng Institute of Technology, Yancheng 224051, P.R. China*

<sup>‡</sup>*Theoretical Physics Department, National Research Centre, Giza12622 Dokki, Egypt*

<sup>¶</sup>*Department of Physics, University of Rome Tor Vergata and INFN, Via della Ricerca Scientifica 1, 00133 Roma, Italy*

<sup>§</sup>*Institute of Physics, University of the Philippines, College, Baños, Laguna 4031 Philippines*

<sup>||</sup>*Center of Basic Science (CBS), Misr University of Science and Technology (MUST), 6th October City, Egypt*

<sup>⊥</sup>*Department of Physics and Astronomy, College of Science, King Saud University, P.O. Box 2455, Riyadh 11451, Saudi Arabia*

<sup>#</sup>*TBpack Ltd., 27 Old Gloucester Street, London, WC1N 3AX, United Kingdom*

<sup>@</sup>*Institute for Nuclear Problems, Belarusian State University, Bobruiskaya 11, 220030 Minsk, Belarus*

E-mail: hazemabdelhameed@gmail.com; domenico.corona@roma2.infn.it; rbpayod@up.edu.ph; mahmoud.sakr@must.edu.eg; omabelkader7@ksu.edu.sa; qfangzhang@gmail.com; vasil.saroka@roma2.infn.it

## Abstract

Two-dimensional topological insulators with propagating topological edge states are promising for dissipationless transport, while their one-dimensional analogs are capable of hosting localized topological junction states that are mainly envisaged for quantum computing and spintronics. Here, in contrast, we propose to use localized nature of topological junction states for sensing applications. We report a systematic topological classification of a wide class of graphene nanoribbons represented by already synthesized extended chevron species. By using this classification, we theoretically model a double-junction transport device that shows enhanced interaction with  $\text{NO}_2$  molecule. Our results show that topological junction states of nanoribbons can open an avenue for topological sensing and junction-assisted chemistry applications.

## Introduction

The exploration of topological states in condensed matter physics has revolutionized our understanding of electronic materials,<sup>1-3</sup> opening new pathways for advanced technological applications.<sup>4</sup> Among the myriads of topologically intriguing systems,<sup>5-7</sup> carbon-based nanostructures played a key role from the very beginning.<sup>8,9</sup> In recent years, particularly graphene nanoribbons (GNRs) have garnered significant attention.<sup>10-22</sup> These one-dimensional (1D) nanostructures, derived from graphene, exhibit unique electronic properties due to their distinct edge terminations and narrow widths.<sup>23,24</sup>

Bulk-boundary correspondence principle is at the heart of the topological band theory of solids. It states that, at the interfaces between regions of different topological orders, topological interface states occur as highly localized electronic modes that are resilient to disorder or perturbations.<sup>1</sup> The topological stability of these interface states can be controlled by several topological invariants. In the case of the integer quantum Hall effect<sup>25,26</sup> or Haldane model,<sup>27</sup> the invariant is the Chern number, while it is  $Z_2$  invariant instead for topological insulators.<sup>8,9</sup> The  $Z_2$  invariant provides the binary classification of topological phases with

values of 0 or 1. A wider classification based on the Chern number utilizes the whole set of integer numbers  $Z$ . In both cases, a zero value stands for a trivial topological order. An interface state appears, whenever two regions with different  $Z$  or  $Z_2$  values meet each other. This basic principle works in all dimensions and has recently attracted a lot of attention for 1D structures, such as graphene nanoribbons, where topological junction states (TJS) have been revealed and classified.<sup>10,11,17,18</sup> The classification of TJS in GNRs can be carried out base on  $Z_2$  invariant<sup>10-12</sup> and also can be generalized by incorporating chiral symmetry and spin corrections.<sup>17</sup> Some of these states have already been experimentally shown and investigated through an atomically precise on-surface bottom-up engineering.<sup>14,15,21,28</sup>

The envisaged applications of topologically protected states are (i) disorder-resilient low-dissipation transport and (ii) robust long-coherence spin states.<sup>2,4</sup> The latter has become a roadmap for topological junction states as potential candidates for designing customizable spintronics<sup>10,13,20</sup> and quantum computing<sup>13,20</sup> nanodevices. Notably, this widely accepted roadmap overlooks chemical sensing, which is arguably a more natural and immediate application. Chemical sensing relies critically on the interaction between the sensor material and the target analyte, where sensitivity and selectivity are paramount.<sup>29</sup> The 1D nature of GNRs, combined with topological junctions providing a high density of localized electronic states to facilitate interaction with chemical species, potentially offers enhanced sensitivity and selectivity that is accessible for readout in a standard transport device similar to a field-effect transistor.<sup>30,31</sup>

This paper presents a theoretical investigation of topological junction states in GNRs, with a particular focus on their application in gas sensing. The gas sensing application has already been proposed and investigated both theoretically<sup>32-35</sup> and experimentally<sup>36,37</sup> for the edge and end states of GNRs; see also a review of more general sensing schemes in Ref. 31. Some experimental studies have demonstrated the detection of volatile compounds such as ethanol and methanol<sup>36</sup> as well as nitrogen dioxide  $\text{NO}_2$ .<sup>37</sup> However, the sensitivity of TJS in GNRs remains unknown. Here, we explore the electronic properties of these

states, their formation mechanisms, and their interaction with  $\text{NO}_2$  as the target molecule. We have noticed that some of the ribbons that we have studied previously<sup>34</sup> (we refer to those as A60 within a more general class of zigzag-shaped GNRs<sup>38-41</sup>), are, in fact, topologically non-trivial. For some combinations of their unit cell structural parameters, they are characterized by the  $Z_2$  invariant derived from the intercellular Zak phase<sup>42,43</sup> calculated in the periodic gauge of the tight-binding (TB) Hamiltonian.<sup>3</sup> Thus, they can form TJSs via seamless combination with a topologically trivial unit cells of armchair GNRs (AGNRs).<sup>10</sup> Performing density functional theory (DFT) calculations to study sensing, we focus on nitrogen dioxide ( $\text{NO}_2$ ) gas, which is a free-radical and a moderate Lewis acid.  $\text{NO}_2$  is an air pollutant affecting the environment and health of people<sup>44,45</sup> and a prototype of a vast range of substances belonging to nitrocompound group, e.g. nitroparaffins and nitroarenes. By leveraging the unique properties of topological junctions in GNRs, we aim to elucidate their potential in creating highly sensitive and selective chemical sensors, paving the way for advancements in environmental monitoring, medical diagnostics, and beyond.

## Results and discussion

### Topological properties

We begin by verifying the TJS theory at the level of nearest-neighbor TB model and by constructing novel junctions. Then we will proceed to the electronic properties investigation within cluster approach of the TB model for the range of constructed junctions.

The TB Hamiltonian of  $\pi$ -electron network is

$$H = \sum_i \varepsilon c_i^\dagger c_i + \sum_{i,j} t_1 \left( c_i^\dagger c_j + \text{h.c} \right) \quad (1)$$

where  $c_i^\dagger$  and  $c_i$  are electron creation and annihilation operators, respectively,  $\varepsilon = 0$  is the on-site energy equal for all lattice sites,  $t_1 = 3.12 \text{ eV}$ <sup>46</sup> is the nearest-neighbor hopping

integral. We note here that  $t_1$  varies for different structures,<sup>47,48</sup> therefore, we will use  $E/t_1$  dimensionless units in what follows. By going into reciprocal  $k$ -space in Eq. (1) via a Fourier transform,  $c_i^\dagger = \frac{1}{\sqrt{N}} \sum_k e^{-ikR_i} c_k^\dagger$  (and similar for  $c_i$ ) with  $N$  being the number of unit cells and  $R_i$  being the site position, we solve the eigenproblem of  $n \times n$  matrix Hamiltonian for a given unit cell of a GNR with  $n$  lattice sites in the cell. Then  $k$ -space Hamiltonian eigenvectors,  $C_i(k) = (C_{i,1}(k), C_{i,2}(k), \dots, C_{i,n}(k))^T$ , can be employed for the calculation of the intercellular Zak phase by Eq. (31) in Ref. 42:

$$\gamma_2 = -\text{Im} \left\{ \log \prod_{j=1}^{N_k} \text{Det} [C_p^\dagger(k_j) C_q(k_{j+1})] \right\}, \quad (2)$$

where  $N_k$  is the number of  $k$ -point sampling the Brillouin zone of the GNR, and the indices  $p$  and  $q$  run from 1 to  $n/2$  so that dot products of eigenvectors in Eq. (2) form a matrix from all occupied states. Here we present the explicit ready-to-use formula for the TB calculations instead of a more common total Zak phase:<sup>10-12,49</sup>  $\gamma = i \int_{\text{BZ}} \langle u_{ik} | \partial_k u_{ik} \rangle$  with  $u_{ik}$  being periodic parts of the Bloch functions. The common definition of the total Zak phase has several practical issues such as irregularity of the complex phase in numerical eigenvectors, peculiarities of valence band crossings, and dependence on the real space origin position and gauge choice.

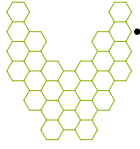
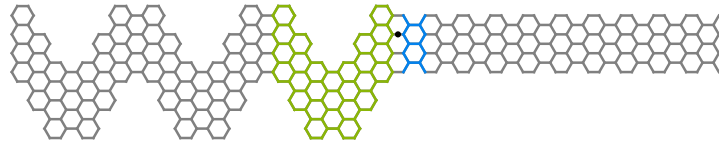
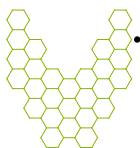
A few comments are worth making before we proceed. First, Eq. (2) must be evaluated on a closed path in  $k$ -space, i.e. on a loop, leading to the same values of  $k_1$  and  $k_{N_k+1}$ . Second, it is also important to impose in Eq. (2) a periodic gauge on the eigenvectors of the Hamiltonian:<sup>42</sup>  $C_i(k + 2\pi/T) = C_i(k)$ , where  $T$  is the translation period of a GNR. Most naturally, this periodic gauge condition is achieved by constructing a *periodic* Hamiltonian in  $k$ -space, i.e. by employing a periodic gauge Hamiltonian based on so-called *basis I*, see Sec. 4.2.5 in Ref. 3 and Ref. 50. Satisfying the two conditions above, the intercellular Zak phase in Eq. (2) is guaranteed to be a well-defined modular  $2\pi$  and independent of the position of the real space origin. This Zak phase, however, depends on the geometry of GNR

unit cell. In this study, the actual Hamiltonian is constructed using TBpack Mathematica application<sup>51</sup> updated with the periodic gauge. We have verified that Eq. (2) reproduces the proposed classification<sup>10</sup> of semiconducting AGNR( $N_p$ ), where  $N_p$  is the number of carbon atom pairs in the unit cell, when all conditions mentioned are met.

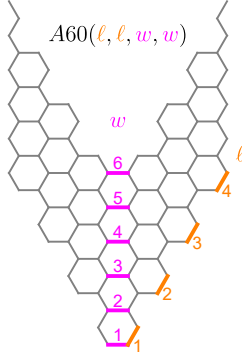
Having equipped with the tools presented above, we can now define  $Z_2 = \text{abs}[\text{mod}(\gamma_2, 2\pi)]$ , where ‘abs’ stands for the absolute value, which is needed because the sign of  $\gamma_2$  is not fixed. The bulk-boundary correspondence for TJS can be verified by constructing finite-size systems that host junctions between (i) two topological unit cells both characterized by  $Z_2 = 1$ , and (ii) one topological unit cell  $Z_2 = 1$  and another trivial unit cell  $Z_2 = 0$ . Taking a unit cell of an AGNR( $N_p$ ), we can seamlessly connect it with some other ribbon. Let us take a chevron GNR (cGNR) and AGNR(7) that both have been synthesized by bottom-up self-assembling method.<sup>52</sup> As shown in Refs. 10,11, the unit cells of cGNR and AGNR(7) can be chosen so that they are either topologically non-trivial,  $Z_2 = 1$ , or not,  $Z_2 = 0$ . We can take cGNR unit cell to be topological, then its connection with a trivial AGNR(7) unit cell must result in a TJS, while a combination with a non-trivial AGNR(7) unit cell must lead to the absence of a TJS. Having connected the two unit cells, we can translate them in opposite directions away from the junction to obtain a finite size system, see Cases 1 and 2 in Table 1. The electronic properties of such a system can be derived from the real space Hamiltonian given by Eq. (1). By employing this cluster approach within the TB model, we are able to track what is happening not only at the junction between the two ribbons but also at the system ends which interface with the vacuum characterized by  $Z_2 = 0$ . For example, when two topological unit cells are linked in the junction, a pair of topological end states (TESs) can arise at the border of each of the ribbons with a trivial vacuum.

Next we consider combinations of AGNR( $N_p$ ) with less known ribbons of A60 class.<sup>38,41</sup> Generically, these ribbons are characterized by a set of structural parameters  $(\ell_1, \ell_2; w_1, w_2)$ , where  $\ell_{1,2}$  stands for arm indices, and  $w_{1,2}$  sets the width vector.<sup>41</sup> We can stick to the mirror symmetric case such that  $\ell_1 = \ell_2 = \ell$  and  $w_1 = w_2 = w$ , see Scheme 1. Within

Table 1: Junctions between various types of GNRs. Light green marks topological structures, while light blue and green-blue - trivial and undefined, i.e. “metallic”, structures, respectively. Black dot is the alignment point for a pair of unit cells forming a junction. Crimson dots show removed dangling atoms from the structure.

Case	Unit cell 1	Unit cell 2	Junction
1 <sup>a</sup>	cGNR $Z_2 = 1$ 	AGNR(7) $Z_2 = 0$ 	cGNR-AGNR(7) 
2 <sup>a</sup>	cGNR $Z_2 = 1$ 	AGNR(7) $Z_2 = 1$ 	cGNR-AGNR(7) 
3	A60(2, 2, 4, 4) $Z_2 = 1$ 	AGNR(7) $Z_2 = 0$ 	A60(2, 2, 4, 4)-AGNR(7) 
4	A60(2, 2, 4, 4) $Z_2 = 1$ 	AGNR(7) $Z_2 = 0$ 	A60(2, 2, 4, 4)-AGNR(7) modified ends 
5	A60(2, 2, 3, 3) $Z_2 = 1$ 	AGNR(5) $Z_2 = \{0, 1\}^b$ 	A60(2, 2, 3, 3)-AGNR(5) 
6 <sup>c</sup>	AGNR(5) $Z_2 = 0; t_{\text{edge}} < t_1$ 	AGNR(5) $Z_2 = 1; t_{\text{edge}} > t_1$ 	AGNR(5)-AGNR(5) 

<sup>a</sup> Junctions previously reported, see Fig. 3(b) in Ref. 11; <sup>b</sup> Ambiguity of  $Z_2$  with respect to applied strain has been reported in Ref. 53; see, for example, Fig. 3(c); Here the structure is considered to be gapless, i.e. metallic one; <sup>c</sup> This junction is obtained by reducing model of Ref. 53, that accounts up to third nearest neighbor hopping interactions.



Scheme 1: The main structural parameters of a mirror symmetric A60 class of GNRs:  $\ell_1 = \ell_2 = \ell$  and  $w_1 = w_2 = w$ .  $A60(\ell_1, \ell_2, w_1, w_2) \implies A60(4, 4, 6, 6)$  is taken as an example. It was synthesized in Ref. 36.

this classification, the extended chevron GNR<sup>36</sup> shall be referred to as  $A60(4, 4; 6, 6)$ . In Table 2, we present the topological properties of A60 ribbons for various values of their structural parameters  $\ell$  and  $w$ . Table 2 provides references, where few species of this class were studied experimentally or theoretically. From Table 2, one sees that  $A60(2, 2; 4, 4)$  with

Table 2:  $Z_2$  topological invariant of  $A60(\ell_1, \ell_2; w_1, w_2)$  GNRs as a function of their structural parameters  $\ell = \ell_1 = \ell_2$  and  $w = w_1 = w_2$ . Lighthgray: A60 GNRs used further in this study. Footnotes: species previously studied in some aspects.

$\ell \setminus w$	3	4	5	6	7	8	9	10	11	12	13	14	15	16	17	18	19	20
2	1	1	0	0	0	1	1	1	0	0	0	1	1	1	0	0	0	1
3	1 <sup>c</sup>	1	0	0 <sup>d</sup>	0	1	1	1	0	0	0	1	1	1	0	0	0	1
4	1	1 <sup>a</sup>	0	0 <sup>b</sup>	0	1	1	1	0	0	0	1	1	1	0	0	0	1
5	1	1	0	0	0	1	1	1	0	0	0	1	1	1	0	0	0	1
6	0	1	0	0	0	1	0	1	0	0	0	1	0	1	0	0	0	1
7	0	1	0	0	0	1	1	1	0	0	0	0	1	1	0	0	0	1
8	0	1	0	0	0	0	0	0	0	0	0	0	0	0	0	0	0	0
9	0	1	0	0	0	1	0	1	0	0	0	0	1	0	0	0	0	0
10	0	1	0	0	0	0	0	0	0	0	0	0	0	0	0	0	0	0

<sup>a</sup> Fig. 2 in Ref. 38; <sup>b</sup> Fig. 2(b) in Ref. 11 and Fig. 1 in Ref. 36; <sup>c</sup> Fig. 2(a,d) in Ref. 34 ; <sup>d</sup> Fig. 2(b,e) in Ref. 34.

$Z_2 = 1$  can be combined with a trivial AGNR(7) with  $Z_2 = 0$  to construct a topological junction. Translating these unit cells into opposite directions, we obtain a finite-size system, as presented by Case 3 in Table 1. Note, however, that ends of the finite system possess carbon atoms with a coordination number equal to 1. In on-surface synthesis, such atoms

will most likely turn into methyl groups with  $sp^3$  hybridization, in contrast to other atoms preserving the  $sp^2$  hybridization of graphene sheet. In this case, the C-C single bond linking the methyl group to the rest of the structure does not contribute to the  $\pi$ -electrons network captured by Eq. (1). That is why we also investigated a structure that is striped from dangling carbon atoms as shown in Case 4 of Table 1.

Within the nearest neighbor TB model, AGNRs described by  $N_p = 3p + 2$ , with  $p$  being an integer, are metallic.<sup>53,54</sup> Strictly speaking Eq. (2) does not give reliable results in this case since is ill-defined for metallic AGNRs. Nevertheless, geometrically nothing prevents us from connecting a metallic AGNR with a topological A60, and this is indeed an instructive example to consider without any reference to the topological band theory. The Case 5 in Table 1 shows a junction between the metallic AGNR(5) and the topological A60(2, 2; 3, 3). Beyond the simplest TB model the AGNR(5) has a tiny gap due to edge relaxation.<sup>53,54</sup> Once such relaxation is modeled by setting the hopping integrals at the edges  $t_{\text{edge}} > t_1$ , Eq. (2) gives  $Z_2$  for gapped AGNR(5) in agreement with the analytical formulae reported in Ref. 10. When relaxation accounted for as small compression of the C-C edge bond is replaced by stretch of the edge bond,  $t_{\text{edge}} < t_1$ , the  $Z_2$  invariant changes its value according to findings of Ref. 53. The same happens for other metallic and gapped AGNRs. Thus, by varying the edge strain, it is possible to construct topological junctions between unit cells of the same shape, as presented by Case 6 in Table 1. The minimal edge strain could probably be achieved even by functionalization of metallic AGNRs with different chemical species along the edges, but for now metamaterial engineering<sup>55-57</sup> seems to be a more viable route towards the edge-strain-based topological junctions.

Figure 1 summarizes the results for the main types of nanoribbon junctions presented in Table 1 and the states observed for them. As one can see from Figure 1a, describing the finite-size structure of Case 1 in Table 1, the zero energy hosts four states, two of which, i.e. No. 195 and 198, are localized at the junction region marked with a vertical dashed black line. These states also have some weight at the trivial end of the structure. This feature is missing

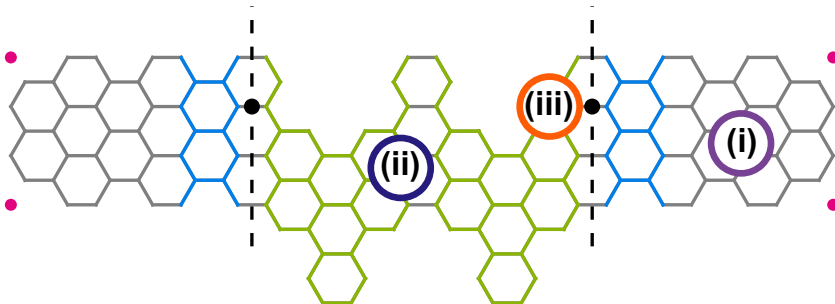
in periodic structure calculations and never mentioned in Ref. 11. The two other states, the highest occupied molecular orbital (HOMO) No. 196 and lowest unoccupied molecular orbital (LUMO) No. 197, are the end states. The state No. 196 is a TES localized at the border of the topological cGNR unit cell and the trivial vacuum, because it can be explained by the bulk-boundary correspondence. In contrast, the state No. 197 unexpectedly forms at the interface between trivial AGNR(7) unit cell (light blue color) and the trivial vacuum which must be an ordinary end state related to dangling carbon atoms as we shall see later. Figure 1b shows the energy levels and the wave functions of the cGNR-AGNR(7) junction, which is Case 2 in Table 1. In this structure, there are only two zero-energy states, which are end states. These HOMO and LUMO states No. 196 and 197, respectively, are both localized at the interface between a topological unit cell and a trivial vacuum. Thus, these states are predicted by the bulk-boundary correspondence principle so that they are both TESs. For comparison, the two bulk states are also presented in Figure 1b. Analogous relations can be noticed in Figure 1c corresponding to Case 3 in Table 1. Here we show electronic energy levels and wave functions for A60(2, 2, 4, 4)-AGNR(7) junction between topological and trivial unit cells, respectively. Similar to Figure 1a, along with the two TJSs, No. 165 and 168, having some weight at the end of the structure, there are states No. 166 and 167 localized entirely at the ends of the structure. To verify the hypothesis that they are merely related to the peculiar dangling C atoms, we constructed Case 4 structure with 5 atoms removed as shown in Table 1. Figure 1d confirms that only one TJS remains after all the dangling C atoms have been removed. Finally, we present the results for the controversial Case 5. We note that Eq. (2) applied to the AGNR(5) yielded  $Z_2 = 1$ . Despite the appeal to interpret the results in Figure 1e with the bulk-boundary correspondence as in the Case 2 discussed with Figure 1b, this approach will not work for other “metallic” structures. Due to this reason, the unit cell of AGNR(5) is highlighted with a blend between light green and light blue colors. On the other hand, when the metallic structure has a well-defined gap due to the edge strain as in Case 6, then a localized TJS is clearly identifiable, as one can see from

Figure 1(f).

In this section, we have seen that topological band theory allows us to predict and reliably construct localized junction states. From a chemistry point of view, these nucleophilic regions with excess electrons due to TJSs are similar to radicals and they must be perfect reaction sites. The geometry of the junction compatible with a standard transport experiment and radical-like nature of the TJS must make them useful for sensing application. Next we investigate this idea at an advanced quantum chemistry level.

## Topological sensing

The above presented junctions are all asymmetric. The asymmetry of the junctions may pose a significant problem for potential transport measurements by requiring differing fabrication approaches of the left and right leads. This problem could be bypassed in a mirror symmetric double junction device (DJD). As shown in Scheme 2, a DJD has a few topological unit cells of an A60 GNR sandwiched between trivial AGNRs.



Scheme 2: The double junction device scheme. Following notation used in Table 1, the light green unit cells of A60(2, 2, 4, 4) are topological ones, while light blue unit cells of AGNR(7) are trivial. The alignment points for the two junctions are depicted with black dots, while the junctions are marked with two dashed black lines. The dangling C atoms that are excluded from  $\pi$ -electron network owing to their conversion into methyl groups are shown as crimson dots. The three circles highlight the chosen site for investigating adsorption properties: (i) violet - AGNR(7), (ii) dark blue - A60(2, 2, 4, 4), and (iii) orange - one of the two topological junctions. Hydrogen atoms are not displayed.

Using DFT calculations as implemented in Gaussian 16<sup>58</sup> and post-processing with *Multi-wfn* software<sup>59</sup> for partial density of states (PDOS) extraction, we scrutinized the electronic

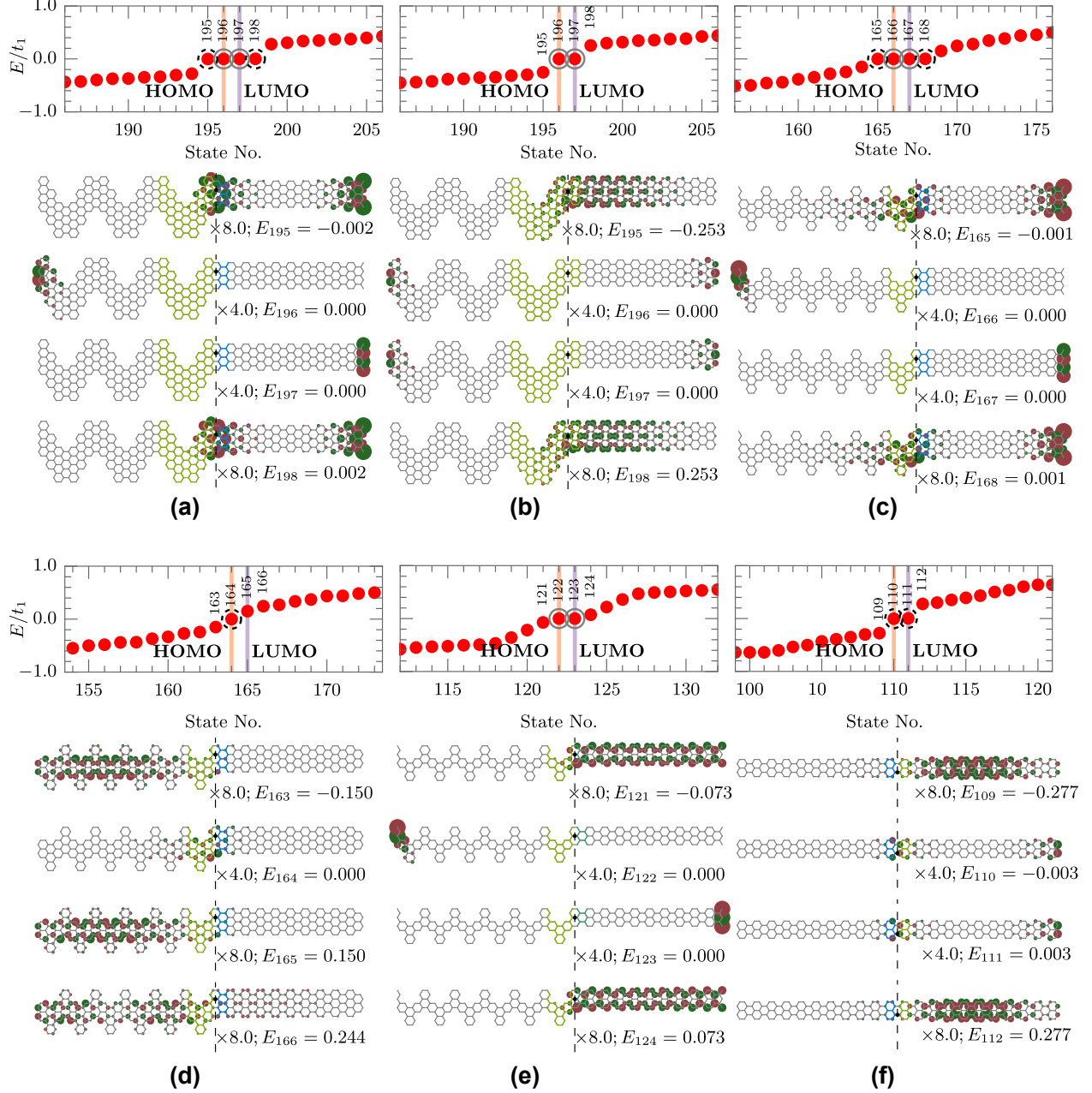


Figure 1: Electronic properties of topological junctions. (a) Energy levels for cGNR-AGNR(7) topological-trivial junction. Vertical orange and violet lines mark HOMO and LUMO, respectively. Dashed black circles highlight TJJs, gray circles highlight end states. The wave functions of the numbered states are presented below, where the scaling factors together with the state energies in terms of  $E/t_1$  are given. Dark red and green show the positive and negative phase of the wave function, respectively. Vertical dashed black lines denote the junction. Black dot is the alignment point for the two underlined unit cells. Light green and light blue highlight topological and trivial unit cells, respectively. (b) Same as (a) but for cGNR-AGNR(7) topological-topological junction. (c) Same as (a) but for A60(2, 2, 4, 4)-AGNR(7) topological-trivial junction. (d) Same as (a) but for A60(2, 2, 4, 4)-AGNR(7) junction with modified ends. (e) Same as (a) but for A60(2, 2, 3, 3)-AGNR(5) ill-defined junction. The green blue color highlights the “metallic” unit cell. (f) Same as (a) but for the edge-strain-induced junction in AGNR(5):  $t_{\text{edge}} = 0.5t_1$  to the left and  $1.5t_1$  to the right of the junction.

and adsorption properties of the DJD. The B3LYP hybrid functional,<sup>60,61</sup> combined with the 6-31G basis set,<sup>62,63</sup> is chosen for modeling due to its efficiency and accuracy with respect to the electronic properties of carbon-based materials.<sup>64-66</sup> Grimme’s Van der Waals correction<sup>67</sup> is applied to the B3LYP functional to account for long-range interactions with the target NO<sub>2</sub> molecule. In the constructed device, the dangling C atoms are properly hydrogenated to form methyl groups, therefore, we expect one TJS per junction similar to Figure 1d. Since two junctions are placed close to each other in our DJD, the two TJS can slightly overlap. This interaction between TJSs shall result in their symmetric splitting around the Fermi energy,  $E_f = 0$  eV, similar to what happens with the ground state of a double quantum well.<sup>68</sup>

As one can see from Figure 2(a), the DFT modeling confirms the expected ground state splitting. The DJD HOMO and LUMO energies are separated by the gap  $E_g = 1.08$  eV. The distributions of the HOMO and LUMO are clearly different from those of the bulk orbitals. While bulk states extend over a large number of trivial AGNR(7) unit cells, the HOMO and LUMO representing TJSs are sharply localized at the two A60(2, 2, 4, 4) unit cells in the region between the two junctions. These topological states are expected to be more interactive than the bulk ones. To compare TJSs to other energy states in the DJD, the reactivity is tested by studying the adsorption properties of the NO<sub>2</sub> gas molecule on different sites of the DJD. In this testing, the NO<sub>2</sub> is initially positioned at 3 Å above the DJD at three sites: (i) the AGNR, (ii) the A60 GNR, and (iii) the junction. Then the whole structure is optimized so that NO<sub>2</sub> ends up at the sites illustrated in Scheme 2. The three chosen adsorption configurations cover reduced electron densities away from the junction and increased electron density due to TJS in the junction region. The adsorption energies in the first two cases are comparable, namely  $-0.27$  and  $-0.30$  eV, respectively. In contrast, the adsorption energy at the junction site is greater than double of these values, i.e.  $E_a = -0.66$  eV. This indicates that TJSs indeed boost interaction with the target molecule. The bond distance analysis suggests that the interaction is mediated by oxygen

atoms. Adsorption of  $\text{NO}_2$  is accompanied by the electron charge transfer of  $-0.54e$  Mulliken charge from the junction to  $\text{NO}_2$  molecule. Before the adsorption, the O-atom charge in  $\text{NO}_2$  molecule is  $-0.19e$  for both oxygen atoms, while N-atom charge is  $0.38e$ . However, these charges decrease to  $-0.41e$  and  $-0.35e$  for oxygen atoms and  $0.22e$  for the nitrogen atom after adsorption at the junction site. Interatomic N-O distances are  $1.19 \text{ \AA}$  and the bond angle is  $134.5^\circ$  before the adsorption. These distances elongate to  $1.30 \text{ \AA}$  and  $1.27 \text{ \AA}$  after adsorption and the angle reduces to  $118.7^\circ$ . For comparison, adsorption of  $\text{NO}_2$  on the A60 and AGNR sites results in  $-0.19e$  and  $-0.11e$  Mulliken charge transfers, respectively. Therefore, physical adsorption at the junction site is stronger than on the other two sites. Figure 2(b) shows spin-polarized energy levels for the system, wherein  $\text{NO}_2$  is adsorbed on the junction spot of the DJD. The main effect of the  $\text{NO}_2$  adsorption is induced spin-splitting of the TJSs, both HOMO and LUMO, and the resulting band gap reduction for spin-down component:  $E_{g,\downarrow} = 0.51 \text{ eV}$ , as compared to  $E_{g,\uparrow} = 1.04 \text{ eV}$  and  $E_g = 1.08 \text{ eV}$  of a non-magnetic case in Figure 2(a). As seen from the HOMO spin-down component, the contribution of  $\text{NO}_2$  into the spin-down component of the bonding HOMO is significant in the case of adsorption at the junction which is compelling evidence of the localized TJSs being more reactive than extended bulk states. The partial densities of states plotted in Figure 2(c) and (d) further demonstrate that  $\text{NO}_2$  contributions (dark blue and violet) into HOMOs are almost vanishing when the adsorption takes place at A60(2, 2, 4, 4) and AGNR(7) sites even though the energy gaps are comparable to the junction case:  $E_{g,\downarrow} = 0.71 \text{ eV}$  and  $0.38 \text{ eV}$  and  $E_{g,\uparrow} = 1.07 \text{ eV}$  and  $1.09 \text{ eV}$ , respectively. This proves that TJSs are suitable for facilitating sensing and catalytic applications.

## Sensor read-out with coherent transport

The constructed symmetric DJD has a favorable configuration for connecting leads to the device and passing a coherent current through it. This current must be sensitive to the electronic properties of the scattering region represented by two junctions between topological

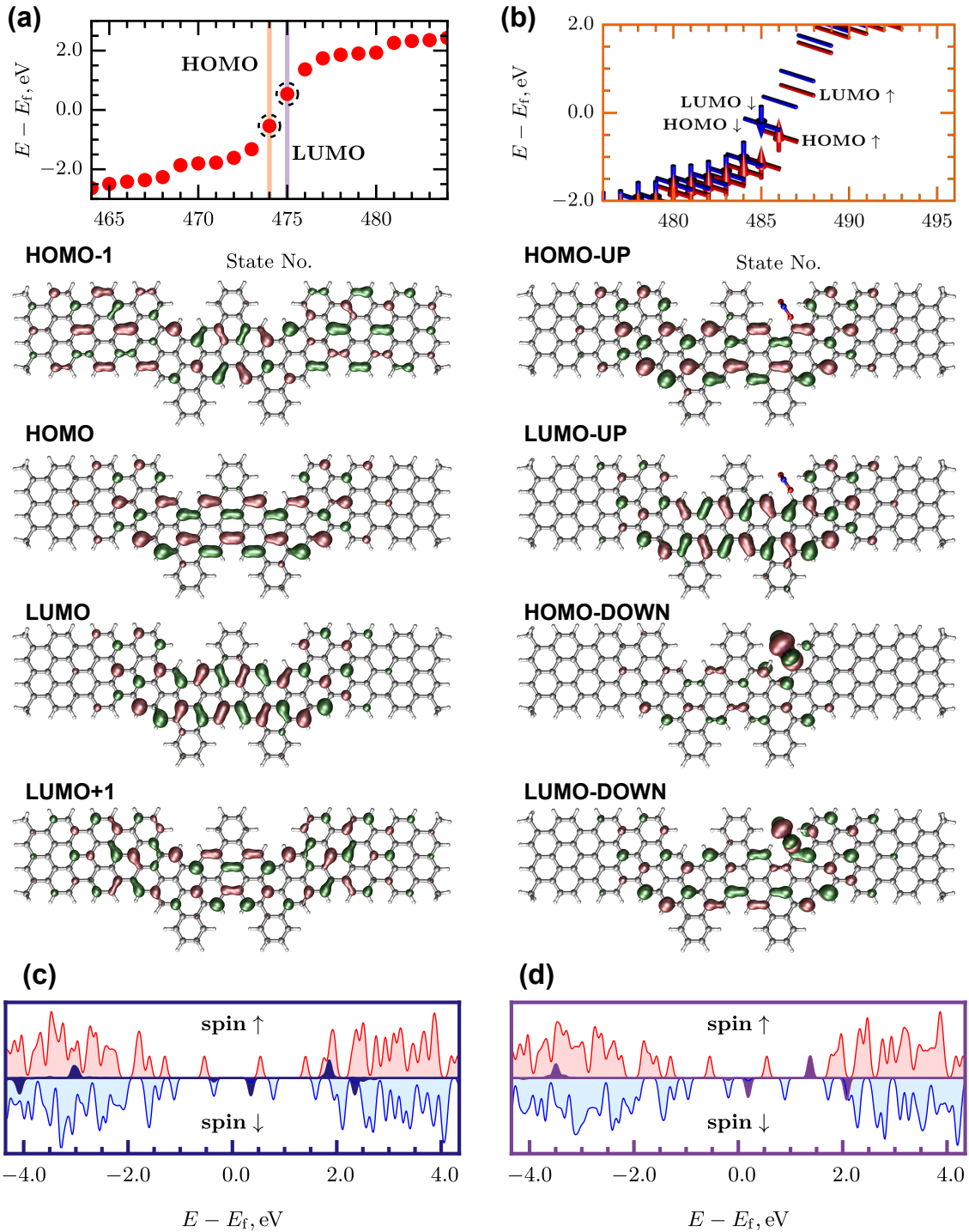


Figure 2: Interaction with  $\text{NO}_2$  gas molecule. (a) The electronic energy levels of pristine DJD together with molecular orbitals of TJS and extended bulk states. Isovalue: 0.02. Similar to Fig. 1 vertical orange and violet lines mark HOMO and LUMO, while dashed black circles highlight TJSs. (b) The spin-polarized electronic energy levels for DJD after adsorption of  $\text{NO}_2$  molecule at the A60(2, 2, 4, 4)-AGNR(7) junction between topological and trivial unit cells. (c) The spin-resolved partial density of states for DJD and  $\text{NO}_2$  molecule adsorbed at A60(2, 2, 4, 4). The  $\text{NO}_2$  data are plotted by the same dark blue color that is used to denote  $\text{NO}_2$  adsorption site in Scheme 2. (d) Same as (c), but for  $\text{NO}_2$  adsorbed at AGNR(7). Broadening: 0.1 eV. The frame colors in (b), (c), and (d) correspond to those of circles showing the adsorption sites in Scheme 2.

and trivial nanoribbon unit cells. The changing current shall be a signature of the physical adsorption happening at the junction. The geometry of the leads is crucial here. In order to facilitate electron injection into the semiconducting structure, we use a combination of topological and chemical engineering. Specifically, we terminate the scattering region with topologically non-trivial AGNR(7) unit cell that has been used in Case 2 of Table 1. In addition, we dope the left and right leads with N-atoms as shown in Figure 3a. The latter may be a bit challenging step from a technological point of view, though the atomically precise doping of GNRs has been demonstrated<sup>69</sup> and N-C interfaces have already been studied experimentally.<sup>70</sup>

The quantum transport through the lead-DJD-lead system is explored using DFT and non-equilibrium Green's function methods implemented in *NanoDCAL* software.<sup>71,72</sup> The local density approximation (LDA) is used for the exchange-correlation functional with an energy cutoff of 160 Ry. The  $k$ -points grid is set to  $1 \times 1 \times 100$  for the leads and  $1 \times 1 \times 30$  for the Brillouin zone. The current passing through the system is determined by Landauer-Büttiker formalism.<sup>73</sup> Thus, we sum the transmission probabilities,  $T = \sum_i T_i$ , for electron states,  $i$ , from one electrode to the other within the energy window subjected to the applied voltage  $V$ :

$$I = \frac{2e}{h} T (\mu_L - \mu_R) , \tag{3}$$

where  $\mu_L - \mu_R = |eV|$ , and the  $\mu_L$  and  $\mu_R$  are the electrochemical potentials of the left and right electrodes, respectively.

In Figure 3b, the current-voltage ( $I$ - $V$ ) characteristics for the DJD-based sensor are presented within a reasonable range of voltages from 0 to 1.6 V. The modeled sensor demonstrates measurable currents of about tens of  $\mu A$ 's. Due to the optimal ratio between the AGNR(7) and A60(2, 2, 4, 4) fragments and the lead engineering, the device is conducting. Longer segments of AGNR(7) show lower conductance in our quantum transport simulations. The adsorption of  $NO_2$  at the favorable junction site results in a twofold increase in current. Simultaneously, the  $NO_2$  adsorption at energetically less favorable sites of AGNR(7)

and A60(2, 2, 4, 4) blocks the current through the sensor. The presented detection mechanism differs from that of the previously proposed junction-free AGNR-based sensors.<sup>74</sup> In our case, the adsorption of the molecule at the junction increases the current, which results in an on-off ratio that is greater than unity, whereas in other schemes the current is usually blocked.

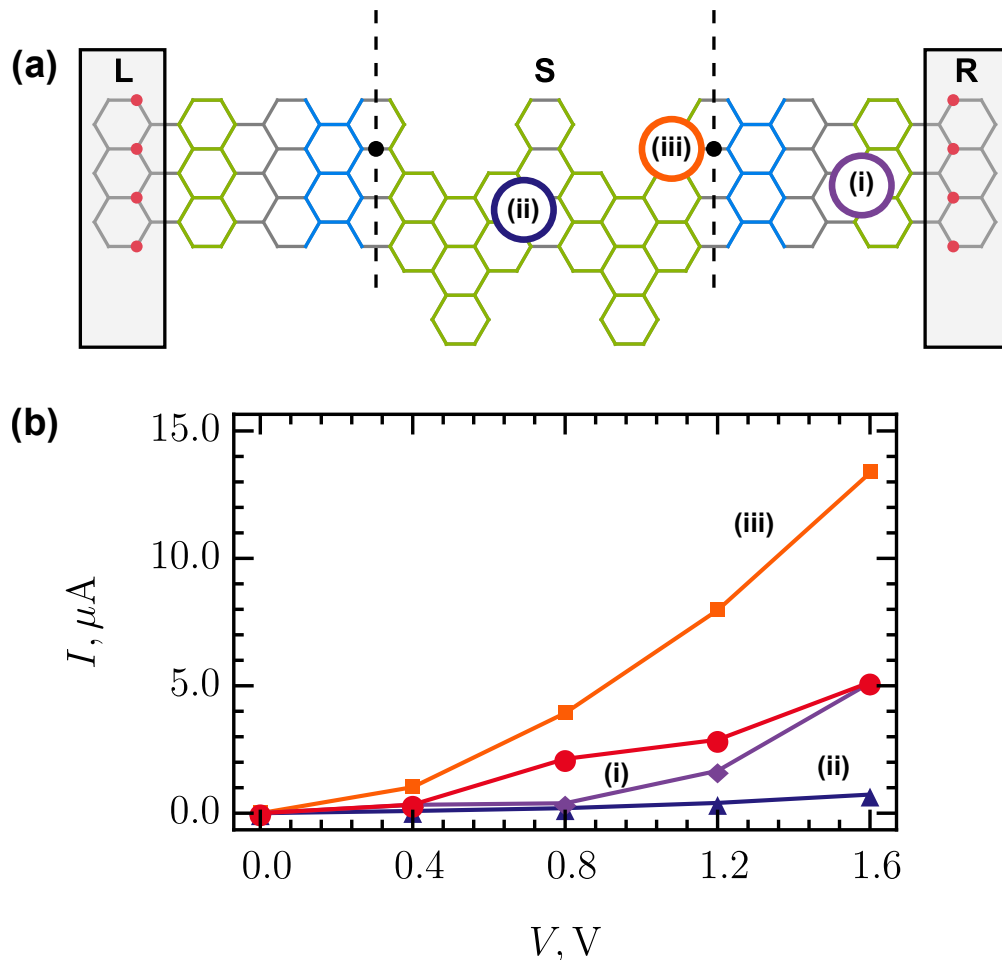


Figure 3: Quantum transport readout of gas molecules. (a) The scheme of the quantum transport sensor. Notations are the same as in Table 1 and Scheme 2. The red dots denote nitrogen atoms. ‘L’, ‘S’, and ‘R’ are the left lead, scattering region, and right lead, respectively. (b) The current-voltage characteristics of the device before and after  $\text{NO}_2$  adsorption: (i) at AGNR(7), (ii) at A60(2, 2, 4, 4), and (iii) the topological junction between A60(2, 2, 4, 4) and AGNR(7) unit cells. The red [disks] are data for pristine sensor, while violet [rhombuses], dark blue [triangles] and orange [squares] are data for the sites that are marked with the same colors in panel (a).

## Conclusions

In summary, we report a systematic topological classification for an A60 class of graphene nanoribbons, some of which have already been synthesized.<sup>36</sup> It is shown that, using this classification, topological junction states can be engineered at the junctions between topological and trivial ribbons. Since these states facilitate charge transfer to NO<sub>2</sub> gas molecule and formation of a polar bond, they can be used in a mirror symmetric double junction configuration as active elements of a gas sensor that is read out by quantum transport measurements. This envisages a niche for sensor applications of topological materials, in addition to the quantum computing perspective suggested in the current literature. In view of the recent advance in an experimental study of topological end states in germanene nanoribbons,<sup>75</sup> we infer that our calculations can also be extended to inorganic chemistry. Another future line of research may be a modeling of homogeneous topological junctions that are induced by edge strain and, therefore, difficult to realize by chemical methods. This could be especially interesting for metamaterials, whereby the localization of junction states could be used to enhance optical and acoustic detections.

## Acknowledgement

The authors thank T. Giovannini for useful discussions and help with some data visualization. This work is supported by the National Natural Science Foundation of China (No. 12274361, No. 12474276). This work is also supported by Researchers Supporting Project (No. RSP2025R468), King Saud University, Riyadh, Saudi Arabia. R.B.P. acknowledges the support from the Institute of Physics, University of the Philippines – Los Baños. V.A.S. was partly supported by HORIZON EUROPE MSCA-2021-PF-01 (Project No. 101065500, TeraExc).

## References

- (1) Hasan, M. Z.; Kane, C. L. Colloquium: Topological insulators. *Rev. Mod. Phys.* **2010**, *82*, 3045–3067.
- (2) Ren, Y.; Qiao, Z.; Niu, Q. Topological phases in two-dimensional materials: a review. *Rep. Prog. Phys.* **2016**, *79*, 066501.
- (3) Cayssol, J.; Fuchs, J. N. Topological and geometrical aspects of band theory. *J. Phys. Mater.* **2021**, *4*, 034007.
- (4) Weber, B. et al. 2024 Roadmap on 2D Topological Insulators. *J. Phys. Mater.* **2024**, *7*, 022501.
- (5) Qi, X.-L. L.; Zhang, S.-C. C. Topological insulators and superconductors. *Rev. Mod. Phys.* **2011**, *83*, 1057–1110.
- (6) Ando, Y. Topological insulator materials. *J. Phys. Soc. Jpn.* **2013**, *82*, 102001.
- (7) Wehling, T.; Black-Schaffer, A.; Balatsky, A. Dirac materials. *Adv. Phys.* **2014**, *63*, 1–76.
- (8) Kane, C. L.; Mele, E. J. Quantum spin Hall effect in graphene. *Phys. Rev. Lett.* **2005**, *95*, 226801.
- (9) Kane, C. L.; Mele, E. J.  $Z_2$  topological order and the quantum spin Hall effect. *Phys. Rev. Lett.* **2005**, *95*, 146802.
- (10) Cao, T.; Zhao, F.; Louie, S. G. Topological phases in graphene nanoribbons: Junction States, spin centers, and quantum spin chains. *Phys. Rev. Lett.* **2017**, *119*, 076401.
- (11) Lee, Y.-I.; Zhao, F.; Cao, T.; Ihm, J.; Louie, S. G. Topological phases in cove-edged and chevron graphene nanoribbons: Geometric structures,  $Z_2$  invariants, and junction states. *Nano Lett.* **2018**, *18*, 7247–7253.

- (12) Lin, K.-S.; Chou, M.-Y. Topological properties of gapped graphene nanoribbons with spatial symmetries. *Nano Lett.* **2018**, *18*, 7254–7260.
- (13) Ortiz, R.; García-Martínez, N. A.; Lado, J. L.; Fernández-Rossier, J. Electrical spin manipulation in graphene nanostructures. *Phys. Rev. B* **2018**, *97*, 195425.
- (14) Rizzo, D. J.; Veber, G.; Cao, T.; Bronner, C.; Chen, T.; Zhao, F.; Rodriguez, H.; Louie, S. G.; Crommie, M. F.; Fischer, F. R. Topological band engineering of graphene nanoribbons. *Nature* **2018**, *560*, 204–208.
- (15) Gröning, O.; Wang, S.; Yao, X.; Pignedoli, C. A.; Borin Barin, G.; Daniels, C.; Cupo, A.; Meunier, V.; Feng, X.; Narita, A.; Müllen, K.; Ruffieux, P.; Fasel, R. Engineering of robust topological quantum phases in graphene nanoribbons. *Nature* **2018**, *560*, 209–213.
- (16) Joost, J. P.; Jauho, A. P.; Bonitz, M. Correlated topological states in graphene nanoribbon heterostructures. *Nano Lett.* **2019**, *19*, 9045–9050.
- (17) Jiang, J.; Louie, S. G. Topology Classification using Chiral Symmetry and Spin Correlations in Graphene Nanoribbons. *Nano Lett.* **2021**, *21*, 197–202.
- (18) Arnold, F. M.; Liu, T.-J.; Kuc, A.; Heine, T. Structure-imposed electronic topology in cove-edged graphene nanoribbons. *Phys. Rev. Lett.* **2023**, *129*, 216401.
- (19) Kuo, D. M. T. Effects of coulomb blockade on the charge transport through the topological states of finite armchair graphene nanoribbons and heterostructures. *Nanomaterials* **2023**, *13*, 1757.
- (20) Perkins, D. T. S.; Ferreira, A. Ultrafast all-electrical universal nanoqubits. *Phys. Rev. B* **2024**, *109*, L041411.
- (21) Wang, Z.; Yin, R.; Tang, Z.; Du, H.; Liang, Y.; Wang, X.; Deng, Q.-S.; Tan, Y.-Z.;

- Zhang, Y.; Ma, C.; Tan, S.; Wang, B. Topologically localized vibronic excitations in second-layer graphene nanoribbons. *Phys. Rev. Lett.* **2024**, *133*, 036401.
- (22) Zhao, C.; Catarina, G.; Zhang, J.-J.; Henriques, J. a. C. G.; Yang, L.; Ma, J.; Feng, X.; Gröning, O.; Ruffieux, P.; Fernández-Rossier, J.; Fasel, R. Tunable topological phases in nanographene-based spin-1/2 alternating-exchange Heisenberg chains. *Nat. Nanotech.* **2024**,
- (23) Yano, Y.; Mitoma, N.; Ito, H.; Itami, K. A quest for structurally uniform graphene nanoribbons: Synthesis, properties, and applications. *J. Org. Chem.* **2020**, *85*, 4–33.
- (24) Chen, Z.; Narita, A.; Müllen, K. Graphene nanoribbons: On-Surface synthesis and integration into electronic devices. *Adv. Mater.* **2020**, *32*, 2001893.
- (25) Simon, B. Holonomy, the quantum adiabatic theorem, and Berry’s phase. *Phys. Rev. Lett.* **1983**, *51*, 2167–2170.
- (26) Niu, Q.; Thouless, D. J.; Wu, Y.-S. Quantized Hall conductance as a topological invariant. *Phys. Rev. B* **1985**, *31*, 3372–3377.
- (27) Haldane, F. D. M. Model for a quantum hall effect without landau levels: Condensed-matter realization of the ”parity anomaly”. *Phys. Rev. Lett.* **1988**, *61*, 2015–2018.
- (28) Wang, S.; Talirz, L.; Pignedoli, C. A.; Feng, X.; Müllen, K.; Fasel, R.; Ruffieux, P. Giant edge state splitting at atomically precise graphene zigzag edges. *Nat. Commun.* **2016**, *7*, 11507.
- (29) Gao, N.; Gao, T.; Yang, X.; Dai, X.; Zhou, W.; Zhang, A.; Lieber, C. M. Specific detection of biomolecules in physiological solutions using graphene transistor biosensors. *Proc. Natl. Acad. Sci. U.S.A.* **2018**, *113*, 14633–14638.

- (30) Adamu, B. I.; Chen, P.; Chu, W. Role of nanostructuring of sensing materials in performance of electrical gas sensors by combining with extra strategies. *Nano Ex.* **2021**, *2*, 042003.
- (31) Johnson, A. P.; Sabu, C.; Swamy, N. K.; Anto, A.; Gangadharappa, H.; Pramod, K. Graphene nanoribbon: An emerging and efficient flat molecular platform for advanced biosensing. *Biosens. Bioelectron* **2021**, *184*, 113245.
- (32) Abdelsalam, H.; Saroka, V. A.; Younis, W. O. Edge functionalization of finite graphene nanoribbon superlattices. *Superlattices Microstruct.* **2019**, *129*, 54–61.
- (33) Čerņevičs, K.; Pizzochero, M.; Yazyev, O. V. Even–odd conductance effect in graphene nanoribbons induced by edge functionalization with aromatic molecules: Basis for novel chemosensors. *Eur. Phys. J. Plus* **2018**, *135*, 681.
- (34) Abdelsalam, H.; Saroka, V.; Teleb, N.; Ali, M.; Osman, W.; Zhang, Q. Electronic and adsorption properties of extended chevron and cove-edged graphene nanoribbons. *Physica E Low Dimens.* **2021**, *126*, 114438.
- (35) Sakr, M. A.; Abdelsalam, H.; Teleb, N. H.; Abd-Elkader, O. H.; Saroka, V. A.; Zhang, Q. Investigating adsorption characteristics and electronic properties of Clar’s goblet and beyond. *Chem. Phys. Lett.* **2024**, *849*, 141428.
- (36) Mehdi Pour, M.; Lashkov, A.; Radocea, A.; Liu, X.; Sun, T.; Lipatov, A.; Korlacki, R. A.; Shekhirev, M.; Aluru, N. R.; Lyding, J. W.; Sysoev, V.; Sinitskii, A. Laterally extended atomically precise graphene nanoribbons with improved electrical conductivity for efficient gas sensing. *Nat. Commun.* **2017**, *8*, 820.
- (37) Cho, K. M.; Cho, S.-Y.; Chong, S.; Koh, H.-J.; Kim, D. W.; Kim, J.; Jung, H.-T. Edge-functionalized graphene nanoribbon chemical sensor: Comparison with carbon nanotube and graphene. *ACS Appl. Mater. Interfaces* **2018**, *10*, 42905–42914.

- (38) Saroka, V. A.; Batrakov, K. G.; Chernozatonskii, L. A. Edge-modified zigzag-shaped graphene nanoribbons: Structure and electronic properties. *Phys. Solid State* **2014**, *56*, 2135–2145.
- (39) Saroka, V. A.; Batrakov, K. G.; Demin, V. A.; Chernozatonskii, L. A. Band gaps in jagged and straight graphene nanoribbons tunable by an external electric field. *J. Condens. Matter Phys* **2014**, *27*, 145305.
- (40) Saroka, V. A.; Batrakov, K. G. In *Physics, Chemistry and Applications of Nanostructures*; Borisenko, V. E., Gaponenko, S. V., Gurin, V. S., Kam, C. H., Eds.; World Scientific: Singapore, 2015; pp 240–243.
- (41) Saroka, V. A.; Batrakov, K. G. Zigzag-shaped Superlattices on the basis of graphene nanoribbons: Structure and electronic properties. *Russ. Phys. J.* **2016**, *59*, 633–639.
- (42) Kudin, K. N.; Car, R.; Resta, R. Berry phase approach to longitudinal dipole moments of infinite chains in electronic-structure methods with local basis sets. *J. Chem. Phys.* **2007**, *126*, 234101.
- (43) Rhim, J.-W.; Behrends, J.; Bardarson, J. H. Bulk-boundary correspondence from the intercellular Zak phase. *Phys. Rev. B* **2017**, *95*, 035421.
- (44) Last, J. A.; Sun, W. M.; Witschi, H. Ozone, NO, and NO<sub>2</sub>: oxidant air pollutants and more. *Environ. Health Perspect.* **1994**, *102*, 179–184.
- (45) Huangfu, P.; Atkinson, R. Long-term exposure to NO<sub>2</sub> and O<sub>3</sub> and all-cause and respiratory mortality: A systematic review and meta-analysis. *Environ. Int.* **2020**, *144*, 105998.
- (46) Partoens, B.; Peeters, F. M. From graphene to graphite: Electronic structure around the K point. *Phys. Rev. B* **2006**, *74*, 075404.

- (47) Saroka, V. A.; Abdelsalam, H.; Demin, V. A.; Grassano, D.; Kuten, S. A.; Pushkarchuk, A.; Pulci, O. Absorption in finite-length chevron-type graphene nanoribbons. *Semiconductors* **2018**, *52*, 1890–1893.
- (48) Payod, R. B.; Grassano, D.; Santos, G. N. C.; Levshov, D. I.; Pulci, O.; Saroka, V. A.  $2N+4$ -rule and an atlas of bulk optical resonances of zigzag graphene nanoribbons. *Nat. Commun.* **2020**, *11*, 82.
- (49) Zak, J. Berry’s phase for energy bands in solids. *Phys. Rev. Lett.* **1989**, *62*, 2747–2750.
- (50) Bena, C.; Montambaux, G. Remarks on the tight-binding model of graphene. *New J. Phys.* **2009**, *11*, 095003.
- (51) Saroka, V. A. TBpack (version 0.4.0 and higher). 2021; <https://github.com/vasilsaroka/TBpack>.
- (52) Cai, J.; Ruffieux, P.; Jaafar, R.; Bieri, M.; Braun, T.; Blankenburg, S.; Muoth, M.; Seitsonen, A. P.; Saleh, M.; Feng, X.; Müllen, K.; Fasel, R. Atomically precise bottom-up fabrication of graphene nanoribbons. *Nature* **2010**, *466*, 470–473.
- (53) Tepliakov, N. V.; Lischner, J.; Kaxiras, E.; Mostofi, A. A.; Pizzochero, M. Unveiling and manipulating hidden symmetries in graphene nanoribbons. *Phys. Rev. Lett.* **2023**, *130*, 9045–9050.
- (54) Son, Y.-W.; Cohen, M. L.; Louie, S. G. Energy gaps in graphene nanoribbons. *Phys. Rev. Lett.* **2006**, *97*, 216803.
- (55) Serra-Garcia, M.; Peri, V.; Süssstrunk, R.; Bilal, O. R.; Larsen, T.; Villanueva, L. G.; Huber, S. D. Observation of a phononic quadrupole topological insulator. *Nature* **2018**, *555*, 342–345.
- (56) Peri, V.; Serra-Garcia, M.; Ilan, R.; Huber, S. D. Axial-field-induced chiral channels in an acoustic Weyl system. *Nat. Phys.* **2019**, *15*, 357–361.

- (57) Xia, S.; Liang, Y.; Tang, L.; Song, D.; Xu, J.; Chen, Z. Photonic realization of a generic type of graphene edge states exhibiting topological flat band. *Phys. Rev. Lett.* **2023**, *131*, 013804.
- (58) Frisch, M. J. et al. Gaussian~16 Revision C.01. 2016; Gaussian Inc. Wallingford CT.
- (59) Lu, T.; Chen, F. Multiwfn: A multifunctional wavefunction analyzer. *J. Comput. Chem.* **2012**, *33*, 580–592.
- (60) Becke, A. D. Density-functional thermochemistry. III. The role of exact exchange. *J. Chem. Phys.* **1993**, *98*, 5648–5652.
- (61) Lee, C.; Yang, W.; Parr, R. G. Development of the Colle-Salvetti correlation-energy formula into a functional of the electron density. *Phys. Rev. B* **1988**, *37*, 785–789.
- (62) Ditchfield, R.; Hehre, W. J.; Pople, J. A. Self-consistent molecular-orbital methods. IX. An extended Gaussian-type basis for molecular-orbital studies of organic molecules. *J. Chem. Phys.* **1971**, *54*, 724–728.
- (63) Hehre, W. J.; Ditchfield, R.; Pople, J. A. Self-consistent molecular orbital methods. XII. Further extensions of Gaussian-type basis sets for use in molecular orbital studies of organic molecules. *J. Chem. Phys.* **1972**, *56*, 2257–2261.
- (64) Povie, G.; Segawa, Y.; Nishihara, T.; Miyauchi, Y.; Itami, K. Synthesis and size-dependent properties of [12], [16], and [24] carbon nanobelts. *J. Am. Chem. Soc.* **2018**, *140*, 10054–10059.
- (65) Abdelsalam, H.; Sakr, M. A.; Saroka, V. A.; Abd-Elkader, O. H.; Zhang, Q. Nanoporous graphene quantum dots constructed from nanoribbon superlattices with controllable pore morphology and size for wastewater treatment. *Surf. Interfaces* **2023**, *40*, 103109.
- (66) Abdelsalam, H.; Abd-Elkader, O. H.; Sakr, M. A. S.; Saroka, V. A.; Zhang, Q. Nanoporous triangulene-based frameworks for the separation of petroleum hydrocar-

- bons: Electronic, magnetic, optical, and adsorption properties. *ACS Appl. Nano Mater.* **2023**, *6*, 15128–15137.
- (67) Grimme, S.; Antony, J.; Ehrlich, S.; Krieg, H. A consistent and accurate *ab initio* parametrization of density functional dispersion correction (DFT-D) for the 94 elements H-Pu. *J. Chem. Phys.* **2010**, *132*, 154104.
- (68) Collier, T. P.; Saroka, V. A.; Portnoi, M. E. Tuning terahertz transitions in a double-gated quantum ring. *Phys. Rev. B* **2017**, *96*, 235430.
- (69) Cai, J.; Pignedoli, C. A.; Talirz, L.; Ruffieux, P.; Söde, H.; Liang, L.; Meunier, V.; Berger, R.; Li, R.; Feng, X.; Müllen, K.; Fasel, R. Graphene nanoribbon heterojunctions. *Nat. Nanotechnol.* **2014**, *9*, 896–900.
- (70) Chen, L. et al. Oriented graphene nanoribbons embedded in hexagonal boron nitride trenches. *Nat. Commun.* **2017**, *8*, 14703.
- (71) Taylor, J.; Guo, H.; Wang, J. *Ab initio* modeling of quantum transport properties of molecular electronic devices. *Phys. Rev. B* **2001**, *63*, 245407.
- (72) Taylor, J.; Guo, H.; Wang, J. *Ab initio* modeling of open systems: Charge transfer, electron conduction, and molecular switching of a C<sub>60</sub> device. *Phys. Rev. B* **2001**, *63*, 121104.
- (73) Datta, S. In *Electronic transport in mesoscopic systems*; Haroon, A., Pepper, M., Broers, A., Eds.; Cambridge University Press: Cambridge, United Kingdom, 1995.
- (74) Tamersit, K. An ultra-sensitive gas nanosensor based on asymmetric dual-gate graphene nanoribbon field-effect transistor: proposal and investigation. *J. Comput. Electron.* **2019**, *18*, 846–855.
- (75) Klaassen, D. J.; Eek, L. A. G.; Rudenko, A. N.; Westende, E. D. v.; Castenmiller, C.; Zhang, Z.; Boeij, P. d.; Houselt, A. v.; Ezawa, M.; Zandvliet, H. J. W.; Smith, C. M.;

Bampoulis, P. Realization of a one-dimensional topological insulator in ultrathin germanene nanoribbons. <http://arxiv.org/abs/2411.18156>.

# TOC Graphic

